

# BaTiO<sub>3</sub> nanotubes by co-axial electrospinning: Rheological and microstructural investigations

*M. Hedayati<sup>a, b</sup>, E. Taheri-Nassaj<sup>a, ✉</sup>, A. Yourdkhani<sup>a</sup>, M. Borlaf<sup>b</sup>, J. Zhang<sup>c</sup>, M. Calame<sup>c</sup>, T. Sebastian<sup>b</sup>, S. Payandeh<sup>d</sup>, F. Clemens<sup>b</sup>*

<sup>a</sup> Department of Materials Engineering, School of Engineering, Tarbiat Modares University, Tehran 14115-143, Iran

<sup>b</sup> Empa, Swiss Federal Laboratories for Materials Science & Technology, Laboratory of High Performance Ceramics, 8600, Dübendorf, Switzerland

<sup>c</sup> Empa, Swiss Federal Laboratories for Materials Science & Technology, Transport at Nanoscale Interfaces Laboratory, 8600, Dübendorf, Switzerland

<sup>d</sup> Empa, Swiss Federal Laboratories for Materials Science & Technology, Laboratory of Materials for Energy Conversion, 8600, Dübendorf, Switzerland

✉ Corresponding author:

[taheri@modares.ac.ir](mailto:taheri@modares.ac.ir)

## Abstract

BaTiO<sub>3</sub> (BT) nanotubes (NT<sub>s</sub>) were synthesized using a co-axial electrospinning process. BT precursor/PVP-ethanol and heavy mineral oil were used as the shell solution and core liquid, respectively. The rheological studies indicated that NT<sub>s</sub> could be formed by a stable jet at a range of viscosities of the shell solution. Due to the shear thinning behavior of the shell solutions, their actual viscosity values at the time of jet formation will be lower than the viscosity of the core liquid. The morphology of the obtained NT<sub>s</sub> was strongly influenced by the viscosity of the shell solution. By increasing the concentration of BT precursor, the morphology of the BT NT<sub>s</sub> was changed from porous to more dense structure. XRD analysis

revealed that the crystallization of BT NT<sub>s</sub> occurs at 550 - 630 °C calcining temperature range. Raman spectra confirmed the presence of tetragonal phase at early stage of crystallization.

Keywords: co-axial electrospinning, nanotubes, viscosity, crystalline structure, BaTiO<sub>3</sub>

## 1. Introduction

Barium titanate (BT) is an extensively studied ferroelectric perovskite type ceramic materials. It is well known for its high dielectric constant, piezoelectric behavior as well as its other properties such as, catalysis, optical and photoluminescence. Due to these properties, BT has found a wide range of applications for using in capacitors [1], transducers [2], actuators [3, 4] flexible sensors [5] electro-optic sensors [6, 7], photocatalysts [8], microwave absorbers [9] and ferroelectric memories [10]. Over the past few decades, nanostructured BT has been under extensive investigation because of the size effects on the ferroelectric and piezoelectric properties as well as the effects of the morphology and shape [11, 12]. Among the different morphologies of nanostructures, considerable attention has been drawn to the one-dimensional (1D) BT such as nano-fibers, nano-rods, nano-wires and nanotubes (NT<sub>s</sub>). This is mainly due to the effect of shape and morphology in 1D form on its different properties especially when the size goes down to nanometer scale [13-15]. As a type of 1D nanomaterials, tubular nanostructures (NT<sub>s</sub>) or hollow nanofibers are having fundamental and technological interest in a variety of areas. NT<sub>s</sub> are able to provide a high surface area to maximize the surface activity and increase the interfacial reactions. These characteristics are beneficial for surface-related applications, e.g., chemical sensors, photocatalysis, electromagnetic wave absorbing and dielectric materials [16-19].

Based on literature, different routes were utilized to fabricate BT NT<sub>s</sub>. Most of these methods are based on bottom-top approaches such as hydrothermal syntheses or liquid phase deposition

(LPD) which could be template-assisted [19-24] or even template free [25, 26]. The other method is the electrospinning, which is mainly a top-down approach. This method has been widely used to produce micro or nanofibers of both polymeric [27-29] and ceramic materials [30-34]. Electrospinning can also be modified and employed to fabricate different kinds of nanofibers with various structures and morphologies such as, porous [35, 36], ribbon [37], helical [38], core/shell [39-41] and hollow [42-44]. Electrospinning is the most efficient and straightforward method to produce inorganic hollow nanofibers (NT<sub>s</sub>). Compared to hydrothermal synthesis, the electrospinning possesses the advantages of larger variety of process parameter to obtain different kinds of nanofibers and nanotubes with a wide range of diameters and lengths. In addition, the production yield is much higher compared to the hydrothermal synthesis. There are several reports on synthesizing BT nanofibers by electrospinning technique for use in different applications [33, 45-49]. Previously, at Empa, electrospinning has been successfully utilized to produce BT [50] and other different ceramic nanofibers [31, 32, 51-54]. However, there are not many reports on fabrication of BT NT<sub>s</sub> by electrospinning specially using co-axial technique. Lee *et al.* [18], prepared hollow porous BT nanofibers by electrospinning method using single capillary. Dan Li *et al.* [42], and Loscertales *et al.* [43] employed the co-axial electrospinning to produce ceramic NT<sub>s</sub>. Two solutions with different viscosities are electrospun at the same time, parameters have to be adjusted to form a stable jet. It is well known that the formation of the hollow nanofiber (NT<sub>s</sub>) and their morphology are strongly dependent on the viscosity of the shell and core solutions. It has been reported that both shell and core liquids must have a minimum viscosity and strength to form a stable core/shell jet [55]. However, a main question still remains: How does the viscosity values of the core and shell solutions affect the formation of stable core/shell fibers during the co-axial electrospinning? In the other words, it is of interest to answer how much the viscosity ratio of the shell to the core solutions should be. Although, there are several reports on synthesizing ceramic NT<sub>s</sub> using co-axial electrospinning, but very few of them have

systematically studied the impact of the viscosity of the solutions on the formation and morphology of NT<sub>s</sub>. Therefore, the main aim of this research is to investigate the effect of viscosities of core and shell solutions on the formation and morphology of BT NT<sub>s</sub>. Effects of calcining temperature on the morphology and crystalline structure of obtained BT NT<sub>s</sub> were also studied in details.

## 2. Experimental procedure

### 2. 1. Solutions preparation

BT NT<sub>s</sub> were prepared by simultaneously electrospinning (co-spinning) of two liquids through a coaxial spinneret. Barium acetate ( $\text{Ba}(\text{CH}_3\text{COO})_2$ , Merck, Germany), acetic acid ( $\text{CH}_3\text{COOH}$ ,  $\geq 99\%$ , Sigma-Aldrich, USA), titanium isopropoxide ( $\text{C}_{12}\text{H}_{28}\text{O}_4\text{Ti}$ , 97%, ABCR GmbH & Co.KG, Germany), were employed to prepare the BT precursor for using in the shell solution. To achieve stoichiometric BT, 1:1 molar ratio of barium acetate and titanium isopropoxide was used. Typically, 2.391 g of barium acetate was fully dissolved in 7.86 g acetic acid at 70 °C for one hour. The solution was then cooled down to 5 °C. After that, 2.655 g of titanium isopropoxide was added dropwise under stirring and kept for 15 h at room temperature. To control the viscosity, a solution of polyvinylpyrrolidone (PVP,  $M_w \approx 1,300,000$ , Sigma-Aldrich, USA) in ethanol (Merck, Germany) was added to the BT precursor solution. PVP/Ethanol solution with different concentrations (7.8, 10 and 12 wt%) were prepared and added in different volume ratios (40 to 70 vol%) to adjust the viscosity. Olive oil (commercial type), linseed oil (Sigma Aldrich, USA) and heavy mineral oil (Sigma Aldrich, USA), were used as the core liquid.

## 2.2. Electrospinning Procedure

The Electrospinning machine, NEU-Pro (NaBond Technologies Co., Limited - China), was used to synthesize NT<sub>s</sub>. The shell solution and oil were loaded in two plastic syringes which are connected to a co-axial spinneret by teflon tubes. The co-axial spinneret was consisting of a smaller (inner) capillary (internal diameter = 0.24 mm) that fits concentrically inside the bigger (outer) capillary (internal diameter = 1.43 mm). The two liquids were injected simultaneously by a precise controllable syringe pump with different feeding rates. The electrospun fibers were collected by a rotating drum covered with an aluminum foil. The electrospinning parameters are given in the Table 1 and the whole process to obtain BT NT<sub>s</sub> is illustrated schematically in Fig. 1.

## 2.3. Calcining process

Before calcining, the oil was extracted by immersing the fibers in octane (Sigma-Aldrich, product of Germany) for 24 hours. After oil removing and drying at 80 °C for 24 h, the green NT<sub>s</sub> were calcined with a heating and cooling rate of 2 °C/min at different temperatures between 500 and 1150 °C for two hours.

## 2. 4. Characterizations

The rheological behavior of shell and core liquids was measured with a Modular Compact Rheometer (MCR 302, Anton Paar GmbH, Austria), using a controlled shear rate program in the range of 1 to 1000 (sec<sup>-1</sup>) at a constant temperature of 25 °C.

The microstructure and morphology of the samples were examined by using a scanning electron microscope (SEM) (Tescan Vega3, Czech Republic) and a transmission electron microscope (TEM) (JEOL – JEM 2200FS, Japan).

Crystalline phase composition of BT NT<sub>s</sub> were analyzed using a X-ray diffractometer (XRD) (PANalytical X'Pert Pro MPD, Netherlands) over 2 $\theta$  range of 10–80° (Cu k $\alpha$ ) and step size of 0.004°. For additional Rietveld refinement, synchrotron radiation X-ray powder diffraction was performed (see Supplemental Information). Raman spectroscopy (Witec alpha 300 R spectrometer, Germany) was carried out on green and different calcined samples using a 488 nm laser beam at the power of 5.144 mW.

Thermogravimetry analysis (TGA) coupled with differential scanning calorimetry (DSC) was performed on green fibers with heating rate of 2 °C/min under air atmosphere from 50 to 1000 °C using a NETZSCH STA 449F3 (Netzsch, Germany). To investigate the DSC peaks, thermal analysis with the same conditions was also done on a sample of electrospun BT nanofibers (NF<sub>s</sub>) prepared according to the another work [50]. For the preparation of NF<sub>s</sub>, the co-axial spinneret was not used.

### 3. Results and Discussion

#### 3.1. Effect of rheological behavior

Fig. 2, represents the viscosity values versus shear rate of three types of oils and shell solutions with different volume percent of three kinds of PVP/Ethanol solutions (7.8, 10 and 12 wt% of PVP). Oils show Newtonian flow behaviour in the applied shear rate range. Moreover, the viscosity of olive and linseed oils is much lower than the heavy mineral oil. Using olive or linseed oil as a core liquid result in jet breakup. This could be attributed to their low viscosity. The jet breakup of the core has been reported before in several studies [55-57]. In fact, the core liquid must have a certain minimum viscosity to be stable during stretching along with the shell solution. According to Loscertales *et al.* [57] in hydrophilic/hydrophobic core/shell solution systems, due to the lower viscosity and higher surface tension, the hydrophilic inner fluid tends to break-up. Li *et al.* [58] reported if a core liquid with low viscosity is used, the resultant fibers

might be beaded. Using the heavy mineral oil the co-axial jet was found to be more stable. The mineral oil has higher viscosity (0.129 Pa.s) and the results are in good agreement with the literature. Therefore, the heavy mineral oil was selected as the core liquid. According to Fig. 2, all the shell solutions represent a slight shear thinning behaviour at higher shear rates. Among these solutions, based on their viscosity values relative to the viscosity of the heavy mineral oil, seven solutions were selected (as listed in Table 2) for electrospinning and further evaluations. To prepare the core/shell nanofibers with continuous and uniform diameters the viscosity ratio of the shell solution to the core liquid must be properly controlled so that, the core and shell liquids can be stretched and elongated at the same magnitude throughout the spinning process. Since the shell solution acts as a guide and surrounds the core liquid, it must be sufficiently viscous. The viscosity of shell solution is directly governed by the molecular weight of PVP and its concentration (or more precisely, the extent of polymer chains entanglements). Using the shell solution comprising 50 vol% of 7.8 wt% PVP solution (sol 1), the jet was unstable and no mat was formed during the co-axial electrospinning. However, using this solution, BT NFs could be successfully prepared by single capillary electrospinning [50]. Generally, during a co-spinning process, the elongation of the shell is mainly created by electrostatic repulsions between the surface charges. Rapid stretching of the shell causes a strong viscous stress, which is then passed onto the core liquid. The shear force stretches the oil phase and elongates it with the shell through mechanisms such as viscous dragging and/or contact friction [58]. Therefore, the viscosity of the shell solution is required to be such that the viscous stress imparted by the shell on the core is sufficient to overcome the interfacial tension between them. This allows the formation of a compound Taylor cone and then a stable jet [56]. The mechanical strength of the shell solution is also important for preparing robust NTs. With increasing the viscosity, the jet become more stable. The shell solution with the highest viscosity (sol 9) was not spinable. Based on our experiments, it was realized that the viscosity of the shell solution should not be too high.

The SEM images in Fig. 3, represents the effects of the viscosity of the shell solutions on the morphology and the size distribution (outer diameter: OD) of the electrospun green hollow fibers obtained from solutions 3, 4, 6, 7 and 8. Using the Sol 3 (with much less viscosity than the mineral oil), despite some hollow fibers can be observed (the inset in the Fig. 3a), but the fibers have beaded structure. Additionally, fibers with the ribbon like morphology can be distinguished. This kind of morphology could be the result of the lack of strength of the shell solution. With increasing the viscosity (using Sol 4), the beaded structure disappeared, the NT<sub>s</sub> morphology became uniform and the average OD increased (Fig. 3b). The larger standard deviation of the mean OD of the electrospun fibers obtained from Sol 3 is related to their beaded and ribbon like morphology. As expected, a larger outer diameter of the NT<sub>s</sub> can be achieved by an increase in the viscosity (Fig. 3c, d and e). Changing the outer diameter (OD) of the as-prepared hollow fibers as a function of the viscosity of the shell solutions is depicted in the Fig. 4. The dashed line shows the viscosity of the heavy mineral oil. The range shown by arrows indicates the viscosity range, which the co-axial jet and hollow fibers could be formed. According to these results, the hollow fibers could be formed at a relatively wide range of the shell solution viscosity (from the solutions with lower viscosities than the mineral oil to those with higher viscosities). It has been already reported that the viscosity of shell solution should be higher than the core liquid as a requirement [59]. However, in the current work, the NT<sub>s</sub> could be formed at a range of viscosities. In electrospinning process, high shear rates on the solution during the ejection of the solution from the nozzle to the jet formation can be expected. Considering the shear thinning behavior of shell solutions (Fig. 2), the viscosity of the shell solution will be always lower in comparison to the core oil. This assumption is in a good agreement with a previous experiments in the co-extrusion process of core – shell fibers [60].

### 3.2. Morphological evaluations and effects of calcining temperature

Fig. 5 and Fig. 6 show the morphology of BT NT<sub>s</sub> obtained from sol 4, 7 and 8, calcined at 850 and 1000 °C, respectively. At 850 °C, all the calcined samples show hollow morphology without any collapse or porosity. By decreasing the vol% of PVP solution in the shell solution (i.e. higher concentration of BT precursor), the OD of NT<sub>s</sub> increases. As shown before in Table 2, even though there is no remarkable difference between the amount of PVP in the sol 4 and 8, the diameter of calcined BT NT<sub>s</sub> obtained from sol 8 is much higher than the NT<sub>s</sub> obtained from sol 4. This indicates that the vol% of PVP solution has a major role on the diameter of calcined BT NT<sub>s</sub>. This is probably due to the presence of more material in the jet at higher concentration. Other researchers have already reported this effect. He *et al.* [61], reported an increase in the fiber diameter with higher shell solution concentration whilst, the concentration of the core solution was kept constant. By increasing calcining temperature to 1000 °C (Fig. 6), the average OD of NT<sub>s</sub> reduces which indicates there is more shrinkage at higher calcining temperatures. Moreover, significant changes occurs in the morphology of NT<sub>s</sub>. It can be seen that BT NT<sub>s</sub> obtained from sol 4 and 7 become highly porous when the calcining temperature increases to 1000 °C. This porous morphology could be the result of the Ostwald ripening of porosities on the surface of NT<sub>s</sub> at higher calcining temperatures. By increasing the calcining temperature, small porosities on the surface of BT NT<sub>s</sub> can connect to each other through the Ostwald ripening effect and form bigger porosities. It was found that with increasing the vol% of PVP solution the porous structure will be more pronounced. When the higher vol% of the lower concentration (wt%) PVP solution was used (i.e. Sol 3), the hollow structure collapsed after annealing at 1000 °C. However, in the case of BT NT<sub>s</sub> obtained from Sol 8, no porous structure is observed at 1000 °C. It seems that the increasing of the concentration of metallic precursor in the shell solution could lead to reduce the formation of porosities and collapse of NT<sub>s</sub>. It might be due to the presence of more ceramic precursor as well as the increase of the wall

thickness of the NT<sub>s</sub>.

Further study of the morphology and microstructure of calcined BT NT<sub>s</sub> was carried out by TEM. Fig. 7, shows the TEM images of calcined (at 1000 °C) BT NT<sub>s</sub> obtained from sol 4 and 7, respectively. The porous morphology with non-uniform wall thicknesses is obvious in these images, which confirm the SEM images in Fig. 6(a, b). Figs. 8 and 9 present the TEM images along with the selected area electron diffraction (SAED) patterns and high resolution (HRTEM) images of lattice fringes of BT NT<sub>s</sub> obtained from sol 8 and calcined at 850 and 1000 °C, respectively. As it is seen, using the lower volume percent (40 vol%) of PVP solution, the morphology of BT NT<sub>s</sub> has altered with more dense and uniform structure. The wall thicknesses of BT NT<sub>s</sub> calcined at both 850 and 1000 °C are uniform, about 41 and 38 nm, respectively. The SAED patterns reveal the polycrystalline structure of individual grains of BT NT<sub>s</sub> obtained at both calcining temperatures. Moreover, the increase in grain size can be easily distinguished at the higher calcining temperature (Fig. 9b) in comparison to the lower temperature (Fig. 8b).

### **3.3. Simultaneous Thermal Analysis of electrospun BT NT<sub>s</sub>**

Fig. 10, represents the DSC-TG curves of the electrospun green BT NF<sub>s</sub> and NT<sub>s</sub> (after oil removing in octane and drying). With increasing temperature, the mass loss of green NT<sub>s</sub> starts sharply at 220 °C and then at 345 °C gradually continues up to 670 °C. In comparison, onset of the mass loss for NF<sub>s</sub> can be detected at 260 °C. Similar to the NT<sub>s</sub>, at around 350°C the mass loss rate decreases until 700°C. The difference between the total mass loss of NT<sub>s</sub> (about 70%) and NF<sub>s</sub> (about 58%) is due to the difference in concentration of PVP in the dried electrospun fiber mats. For green NT<sub>s</sub>, there are three obvious exothermic DSC peaks in the temperature range of 200 to 400 °C while for NF<sub>s</sub>, there is just one sharp exothermic peak at this temperature range. The sharp peak at 220 °C correlates with the ignition and decomposition

of residual octane in green NT<sub>s</sub>. The second peak at 320 °C corresponds to the decomposition of PVP and barium acetate [46, 62]. This DSC peak is also present in the green NF<sub>s</sub>. The third peak at 400 °C is related to the decomposition of residual mineral oil. The exothermic peak, which starts at around 525 °C and ends at 630 °C is related to the crystallization of BaTiO<sub>3</sub>. Based on the TG experiments, there is no obvious weight loss after 650 °C. Therefore, it can be concluded that the decomposition of organic groups from the organometallic precursor (titanium isopropoxide) and its intermediate compounds (titanium isopropoxide acetate) is completed at around 650 °C [63].

### 3.4. Crystalline Structure

The XRD patterns of green and calcined BT NT<sub>s</sub> at different temperatures are presented in Fig. 11. As expected, the green NT<sub>s</sub> exhibit amorphous structure. For the samples calcined at 500 °C, none of the Bragg diffractions of BT are observed and the visible peaks might be for oxalate hydrate of barium titanium oxide or barium carbonates induced by unreacted intermediate phase. [64-66]. With increasing calcining temperature to 550 °C, the diffraction peaks of BT start to appear. At 600 °C, all the diffraction peaks of BT are appeared and it becomes the dominant phase. Increasing the calcination temperature to 630 °C, the diffraction peak at 26° (corresponds to BaCO<sub>3</sub>) disappeared and BT diffraction peaks become more pronounced. Correlating the XRD and TG-DSC data demonstrates that the crystallization of BT occurs within 550-630 °C temprature range.

Increasing the calcination temperature to 950 °C, does not cause any changes in the shape of the peaks and the sample becomes more crystalline. A further nominal increase in the calcination temperature to 975 °C, the peak splitting shows up. Usually, the splitting of (200) planes to (002) and (200) (around  $2\theta = 45^\circ$ ) which is a result of the distortion of the unit cell, is considered as the identifier for the tetragonal phase of BT. At 1000 and 1150 °C, splitting is

more clear and reflections become sharper demonstrating the crystallinity enhancement. The lack of observable peak splitting in the samples calcined up to 950 °C cannot be considered as an evidence of the cubic BT. Because, the difficulties with the observation of the tetragonal phase in nanograins by XRD can be explained by peak broadening effect due to the low  $c/a$  ratio in the tetragonal BT. The tetragonal phase of BT has  $P4mm$  symmetry with a tetragonality ( $c/a$  ratio) close to one. Therefore, the differences in cell parameters between cubic and tetragonal phases are small in comparison with other sources of broadening in the XRD pattern. Particularly, when the crystallite size is in the nanoscale, any small splitting can be obscured by peak broadening effect. Therefore, it is usually difficult to distinguish the tetragonal from the cubic phase using the X-ray powder diffraction measurements [67-69]. Using even the synchrotron radiation performed on samples calcined at 950, 975 and 1000 °C, no peak splitting was observed for sample calcined at 950 °C (Supplemental information Fig. S1). However, our calculations using Rietveld refinements revealed small tetragonality at lower temperatures. Fig. 12 is showing the effect of calcining temperature on the tetragonality of BT NT<sub>s</sub> and the average crystallite size (calculated by Scherrer equation). As the calcining temperature increases from 750 °C to 950 °C, the crystallite size increases from about 22 to 31 nm and tetragonality increases from 1.0017 to 1.0041. This increase in crystallite size is attributed to the grain growth with increasing the calcining temperature. From 950 to 975 °C, the crystallite size increases significantly to 63 nm and the  $c/a$  ratio increases to 1.0075. A further increase in the crystallite size (from 63 to 87 nm), and a further increase in  $c/a$  ratio to 1.0097 can be observed when increasing calcination temperature from 975 to 1000 °C. This increasing of grain size might be due to the beginning of the sintering stage at 950 °C [31]. Calcination at 1150 °C, caused the crystallite size of 95 nm, which is mainly due to the grain coarsening whilst the tetragonality is about 1.010. Similar results have been found by Smith *et al.* [67] and Hoshina *et al.* [70]. They showed a decrease of the  $c/a$  axis ratio of tetragonal BT with a decrease of the particle size to nanometer dimensions.

Raman spectroscopy was employed to gain more insight about the effect of calcining temperature on the crystalline structure of BT NT<sub>s</sub>. Fig. 13, shows Raman spectra of as-spun (green NT<sub>s</sub>) and different calcined BT NT<sub>s</sub>. To be able to identify the Raman active modes, the spectra of green and calcined fibers up to 650 °C are shown separately as an inset. It is obvious that there is no Raman characteristic peak of BT in as-spun green fibers. For calcined BT NT<sub>s</sub>, the relevant peaks of tetragonal BT can be observed even at the early stage of crystallization (i.e. at 550 °C). The tetragonal BT in the *P4mm* symmetry has eight Raman active modes represented by  $4E(\text{TO} + \text{LO}) + 3A_1(\text{TO} + \text{LO}) + B_1(\text{TO} + \text{LO})$ . All calcined BT NT<sub>s</sub> samples show the characteristic bands of the tetragonal structure at about 263, 305, 520 and 720 cm<sup>-1</sup>. The most important characteristic peaks of tetragonal BT are the bands at 305 cm<sup>-1</sup> (which indicates the asymmetry within tetragonal distortion of TiO<sub>6</sub> octahedral) and 720 cm<sup>-1</sup>. For cubic structure, even though the symmetry group does not predict Raman active modes, two broad bands at about 250 and 520 cm<sup>-1</sup> could be observed [71, 72]. The weak band at 185 cm<sup>-1</sup> ( $A_1(\text{TO})$ ) and a negative dip at 180 cm<sup>-1</sup> ( $E(\text{TO}), E(\text{LO})$ ) could be also assigned to tetragonal BT [73]. Based on Fig. 13, it is obvious that calcining temperature affects the intensity of the characteristic bands, significantly. It is also seen that the intensity of spectra of samples calcined at temperatures less than 950 °C is much lower compared to those of calcined at this temperature and higher (975 and 1000 °C).

A significant increase in peak intensity occurs at calcination temperature of 1000 °C. The increase of the Raman band intensity with increasing the calcination temperature could be related to the increase of the tetragonality (as it was shown before in Fig. 12). Raman spectra revealed the existence of some other crystalline phases, which cannot be observed by XRD or even synchrotron patterns. In the spectrum of the sample calcined at 1000 °C, a peak shoulder is appeared at around 469 cm<sup>-1</sup> (indicated by arrow in Fig. 13). This can be explained by the present of rhombohedral phase [71, 72]. The small Raman band at 640 cm<sup>-1</sup> (indicated by H in Fig. 13), and a very weak peak at 153 cm<sup>-1</sup>, indicate the present of high temperature hexagonal phase of

BT. These peaks are observed at samples calcined at 550 to 750 °C and disappeared at higher calcination temperatures.. The coexistence of the metastable hexagonal phase with stable tetragonal phase of BT at room temperature has been previously reported by Yashima et al. [68] and Gajović et al. [74]. The hexagonal to tetragonal phase transition in BT is reconstructive. This type of transformation is characterized by slow kinetics. Therefore, it is expected that with increasing the calcination temperature and increase of tetragonal phase, the amount of hexagonal decreases.

#### 4. Conclusion

The above results and discussion can be concluded as follows:

- The viscosities of both shell and core solutions have a major effect on the spinability and formation of core-shell fibers. The viscosity of core liquid should not be too low. To create uniform core-shell fibers by co-axial electrospinning, the shell solution must have enough viscosity and strength, which can be adjusted by controlling the vol% and concentration of PVP/Ethanol solution.
- Based on the presented results and previous experiences, it is expected that the actual value of the viscosity of the shell solution at the time of jet formation should be lower than the viscosity of the heavy mineral oil.
- To achieve BT NT<sub>s</sub> with desired morphology and diameter size, a precise combination of viscosity and concentration of the BT precursor in the shell solution should be selected. To obtain the BT NT<sub>s</sub> with almost non-porous morphology at high temperature (i.e. 1000 °C), the use of higher concentration of BT precursor is suggested.
- Crystallization of BT NT<sub>s</sub> occurs in tetragonal structure at a temperature range between 550 and 630 °C. With increasing the calcining temperature, the tetragonality increases.

#### Declaration of interests

The authors declare that they have no known competing financial interests or personal relationships that could have appeared to influence the work reported in this paper.

## Acknowledgments

This work was financial supported by the Ministry of Science, Research and Technology of Iran. The authors would like to thank Dr. Yadira Arroyo (Electron Microscopy Center, Empa) for her useful help and discussion for analyzing SAED patterns. We would also like to show our gratitude to Dr. Lovro Gorjan (Laboratories for high performance ceramics) for his kindness to do thermal analyses. They would also appreciate the Empa internal funding and SNF project No. 206021 164024 for financing the new instrument (DSC-TGA). The EMPAPOSTDOCS-II program from the European Union's Horizon 2020 research and innovation program under the Marie Skłodowska-Curie grant agreement number 754364 is also appreciated

## References

- [1] G. Yang, Z. Yue, J. Zhao, H. Wen, X. Wang, L. Li, Dielectric behaviour of BaTiO<sub>3</sub>-based ceramic multilayer capacitors under high dc bias field, *J. Phys. D: Appl. Phys.* 39(16) (2006) 3702-3707.
- [2] K.-i. Kakimoto, K. Fukata, H. Ogawa, Fabrication of fibrous BaTiO<sub>3</sub>-reinforced PVDF composite sheet for transducer application, *Sensor Actuat. A-Phys.* 200 (2013) 21-25.
- [3] J. Gao, D. Xue, W. Liu, C. Zhou, X. Ren, Recent progress on BaTiO<sub>3</sub>-based piezoelectric ceramics for actuator applications, *Actuators* 6(3) (2017) 24.
- [4] M. Acosta, N. Novak, V. Rojas, S. Patel, R. Vaish, J. Koruza, G.A. Rossetti, J. Rödel, BaTiO<sub>3</sub>-based piezoelectrics: Fundamentals, current status, and perspectives, *Appl. Phys. Rev.* 4(4) (2017) 041305.
- [5] T. Sebastian, T. Lusiola, F. Clemens, Ferroelectric hybrid fibers to develop flexible sensors for shape sensing of smart textiles and soft condensed matter bodies, *Smart Mater. struct.* 26(4) (2017) 045003.

- [6] P. Castera, D. Tulli, A.M. Gutierrez, P. Sanchis, Influence of BaTiO<sub>3</sub> ferroelectric orientation for electro-optic modulation on silicon, *Opt. Express* 23(12) (2015) 15332-42.
- [7] Y. He, T. Zhang, W. Zheng, R. Wang, X. Liu, Y. Xia, J. Zhao, Humidity sensing properties of BaTiO<sub>3</sub> nanofiber prepared via electrospinning, *Sensor Actuat. B-Chem.* 146(1) (2010) 98-102.
- [8] S. Kappadan, T.W. Gebreab, S. Thomas, N. Kalarikkal, Tetragonal BaTiO<sub>3</sub> nanoparticles: An efficient photocatalyst for the degradation of organic pollutants, *Mat Sci Semicon Proc* 51 (2016) 42-47.
- [9] Z. Ma, C. Cao, J. Yuan, Q. Liu, J. Wang, Enhanced microwave absorption of BaTiO<sub>3</sub>-based ferroelectric/ferromagnetic nanocomposite, *Appl. Surf. Sci.* 258(19) (2012) 7556-7561.
- [10] C.H. Seager, D.C. McIntyre, W.L. Warren, B.A. Tuttle, Charge trapping and device behavior in ferroelectric memories, *Appl. Phys. Lett.* 68(19) (1996) 2660-2662.
- [11] L. Mitoseriu, L.P. Curecheriu, Nanostructured barium titanate ceramics -intrinsic versus extrinsic size effects, in: Miguel Algueró, J. Marty Gregg, L. Mitoseriu (Eds.), *Nanoscale ferroelectrics and multiferroics: key processing and characterization issues, and nanoscale effects*, John Wiley & Sons, Ltd. 2016, pp. 473-511.
- [12] M.J. Polking, M.G. Han, A. Yourdkhani, V. Petkov, C.F. Kisielowski, V.V. Volkov, Y. Zhu, G. Caruntu, A.P. Alivisatos, R. Ramesh, Ferroelectric order in individual nanometre-scale crystals, *Nat. Mater.* 11(8) (2012) 700-9.
- [13] N. Bao, L. Shen, A. Gupta, A. Tatarenko, G. Srinivasan, K. Yanagisawa, Size-controlled one-dimensional monocrystalline BaTiO<sub>3</sub> nanostructures, *Appl. Phys. Lett.* 94(25) (2009) 253109.
- [14] J. Hong, D. Fang, Size-dependent ferroelectric behaviors of BaTiO<sub>3</sub> nanowires, *Appl. Phys. Lett.* 92(1) (2008) 012906.

- [15] Z. Wang, A.P. Suryavanshi, M.-F. Yu, Ferroelectric and piezoelectric behaviors of individual single crystalline BaTiO<sub>3</sub> nanowire under direct axial electric biasing, Appl. Phys. Lett. 89(8) (2006) 082903.
- [16] X. Zhu, Z. Liu, N. Ming, Perovskite oxide nanotubes: synthesis, structural characterization, properties and applications, J. Mater. Chem. 20(20) (2010) 4015.
- [17] Z.H. Lin, Y. Yang, J.M. Wu, Y. Liu, F. Zhang, Z.L. Wang, BaTiO<sub>3</sub> Nanotubes-Based Flexible and Transparent Nanogenerators, J. Phys. Chem. Lett. 3(23) (2012) 3599-604.
- [18] K. Woong Lee, K. Siva Kumar, G. Heo, M.-J. Seong, J.-W. Yoon, Characterization of hollow BaTiO<sub>3</sub> nanofibers and intense visible photoluminescence, J. Appl. Phys. 114(13) (2013) 134303.
- [19] W. Liming, D. Xiangyun, L. Jianbao, L. Xinxing, Z. Guoqing, W. Chunpeng, S. Kuifan, Hydrothermal synthesis of tetragonal BaTiO<sub>3</sub> nanotube arrays with high dielectric performance, J. Nanosci. Nanotechnol. 14(6) (2014) 4224-4228.
- [20] F. Zhang, S.G. Chen, Y.S. Yin, C.R. Xue, C. Lin, Hydrothermal synthesis of BaTiO<sub>3</sub> nanotubes on Ti substrates, Adv. Mat. Res. 79-82 (2009) 617-620.
- [21] J. Yang, L.J. Wang, X.Y. Deng, J. Shao, Y.S. Sun, X.G. Hou, The hydrothermal synthesis of BaTiO<sub>3</sub> nanotubes arrays with good electrical property, Adv. Mat. Res. 873 (2013) 158-163.
- [22] A. Lamberti, N. Garino, F. Bella, K. Bejtka, S. Bianco, D. Manfredi, E. Ambrosio, M. Lombardi, C.F. Pirri, M. Quaglio, BaTiO<sub>3</sub> nanotube arrays by hydrothermal conversion of TiO<sub>2</sub> nanotube carpets grown by anodic oxidation, 64th Annual Meeting of the International Society of Electrochemistry, 2013.
- [23] Y. Yang, X. Wang, C. Sun, L. Li, Structure study of single crystal BaTiO<sub>3</sub> nanotube arrays produced by the hydrothermal method, Nanotechnology 20(5) (2009) 055709.
- [24] A. Yourdkhani, D. Caruntu, M. Vopson, G. Caruntu, 1D core-shell magnetoelectric nanocomposites by template-assisted liquid phase deposition, Cryst. Eng. Comm. 19(15) (2017) 2079-2088.

- [25] Y.F. Zhu, L. Zhang, T. Natsuki, Y.Q. Fu, Q.Q. Ni, Facile synthesis of BaTiO<sub>3</sub> nanotubes and their microwave absorption properties, *ACS Appl. Mater. Interfaces* 4(4) (2012) 2101-6.
- [26] Y. Mao, S. Banerjee, S.S. Wong, Hydrothermal synthesis of perovskite nanotubes, *Chem. Commun.* (3) (2003) 408-409.
- [27] A. Baji, Y.-W. Mai, S.-C. Wong, M. Abtahi, P. Chen, Electrospinning of polymer nanofibers: Effects on oriented morphology, structures and tensile properties, *Compos. Sci. Technol.* 70(5) (2010) 703-718.
- [28] F. Mokhtari, M. Latif, M. Shamshirsaz, Applying the genetic algorithm for determination electrospinning parameters of poly vinylidene fluoride (PVDF) nanofibers: theoretical & experimental analysis, *Journal of Textile Engineering & Fashion Technology (JTEFT)* 3(3) (2017).
- [29] Z.-M. Huang, Y.Z. Zhang, M. Kotaki, S. Ramakrishna, A review on polymer nanofibers by electrospinning and their applications in nanocomposites, *Compos. Sci. Technol.* 63(15) (2003) 2223-2253.
- [30] X. Shi, W. Zhou, D. Ma, Q. Ma, D. Bridges, Y. Ma, A. Hu, Electrospinning of nanofibers and their applications for energy devices, *J. Nanomater.* 2015 (2015) 1-20.
- [31] T. Lusiola, L. Gorjan, F. Clemens, Preparation and characterization of potassium sodium niobate nanofibers by electrospinning, *Int. J. Appl. Ceram. Technol.* 15(5) (2018) 1292-1300.
- [32] M. Mohammadi, P. Alizadeh, F.J. Clemens, Synthesis of CaCu<sub>3</sub>Ti<sub>4</sub>O<sub>12</sub> nanofibers by electrospinning, *Ceram. Int.* 41(10) (2015) 13417-13424.
- [33] J. Yuh, J.C. Nino, W.M. Sigmund, Synthesis of barium titanate (BaTiO<sub>3</sub>) nanofibers via electrospinning, *Mater. Lett.* 59(28) (2005) 3645-3647.
- [34] T. Lusiola, F. Clemens, Fabrication of one-dimensional ferroelectric nano- and microstructures by different spinning techniques and their characterization, in: M. Alguero', J.M. Gregg, L. Mitoseriu (Eds.), *Nanoscale ferroelectrics and multiferroics: key processing and characterization issues and nanoscale effects*, John Wiley & Sons, Ltd. 2016.

- [35] J.T. McCann, D. Li, Y. Xia, Electrospinning of nanofibers with core-sheath, hollow, or porous structures, *J. Mater. Chem.* 15(7) (2005) 735.
- [36] S.P. Adhikari, H.R. Pant, H.M. Mousa, J. Lee, H.J. Kim, C.H. Park, C.S. Kim, Synthesis of high porous electrospun hollow TiO<sub>2</sub> nanofibers for bone tissue engineering application, *J. Ind. Eng. Chem.* 35 (2016) 75-82.
- [37] A.V. Stanishevsky, J.D. Wetuski, H. Yockell-Lelièvre, Crystallization and stability of electrospun ribbon- and cylinder-shaped tungsten oxide nanofibers, *Ceram. Int.* 42(1) (2016) 388-395.
- [38] H. Wu, S. Zhao, W. Ding, L. Han, Studies of interfacial interaction between polymer components on helical nanofiber formation via Co-electrospinning, *Polymers* 10(2) (2018) 119.
- [39] Y. Li, J. Liu, J.R. de Bruyn, W. Wan, Optimization of the electrospinning process for core-shell fiber preparation, *J. Biomater. Tissue Eng* 4(11) (2014) 973-980.
- [40] Jian H. Yu, Sergey V. Fridrikh, G.C. Rutledge, Production of submicrometer diameter fibers by two-fluid electrospinning, *Adv. Mater. Res.* 16(17) (2004) 1562-1566.
- [41] J. Rajala, H. Shin, D. Lolla, G. Chase, Core-Shell electrospun hollow aluminum oxide ceramic fibers, *Fibers* 3(4) (2015) 450-462.
- [42] Dan Li, Y. Xia, Direct fabrication of composite and ceramic hollow nanofibers by electrospinning, *Nano Lett.* 4(5) (2004) 933-938.
- [43] Ignacio G. Loscertales, Antonio Barrero, Manuel Márquez, Rubén Spretz, Raffet Velarde-Ortiz, G. Larsen, Electrically forced coaxial nanojets for one-step hollow nanofiber design, *J. Am. Chem. Soc.* 126(17) (2004) 5376-5377.
- [44] C. Niu, J. Meng, X. Wang, C. Han, M. Yan, K. Zhao, X. Xu, W. Ren, Y. Zhao, L. Xu, Q. Zhang, D. Zhao, L. Mai, General synthesis of complex nanotubes by gradient electrospinning and controlled pyrolysis, *Nature communications* 6 (2015) 7402.

- [45] J.T. McCann, J.I.L. Chen, D. Li, Z.-G. Ye, Y. Xia, Electrospinning of polycrystalline barium titanate nanofibers with controllable morphology and alignment, *Chem. Phys. Lett.* 424(1-3) (2006) 162-166.
- [46] B. Sahoo, P.K. Panda, Preparation and characterization of barium titanate nanofibers by electrospinning, *Ceram. Int.* 38(6) (2012) 5189-5193.
- [47] F. Wang, Y.-W. Mai, D. Wang, R. Ding, W. Shi, High quality barium titanate nanofibers for flexible piezoelectric device applications, *Sensor Actuat. A-Phys.* 233 (2015) 195-201.
- [48] A. Baji, Y.-W. Mai, Q. Li, Y. Liu, Nanoscale investigation of ferroelectric properties in electrospun barium titanate/polyvinylidene fluoride composite fibers using piezoresponse force microscopy, *Compos. Sci. Technol.* 71(11) (2011) 1435-1440.
- [49] Y. Song, Y. Shen, H. Liu, Y. Lin, M. Li, C.-W. Nan, Enhanced dielectric and ferroelectric properties induced by dopamine-modified BaTiO<sub>3</sub> nanofibers in flexible poly(vinylidene fluoride-trifluoroethylene) nanocomposites, *J. Mater. Chem.* 22(16) (2012) 8063.
- [50] T. Sebastian, A. Michalek, M. Hedayati, T. Lusiola, F. Clemens, Enhancing dielectric properties of barium titanate macrofibers, *J. Eur. Ceram. Soc.* 39(13) (2019) 3716-3721.
- [51] F.A. Berutti, A.K. Alves, F.J. Clemens, T. Graule, C.P. Bergmann, Electrospinning and characterisation of ceria doped yttria fibres, *Adv. Appl. Ceram.* 109(1) (2013) 62-64.
- [52] D. Regonini, A.C. Teloeken, A.K. Alves, F.A. Berutti, K. Gajda-Schranz, C.P. Bergmann, T. Graule, F. Clemens, Electrospun TiO<sub>2</sub> fiber composite photoelectrodes for water splitting, *ACS Appl. Mater. Interfaces* 5(22) (2013) 11747-55.
- [53] A.K. Alves, F.A. Berutti, F.J. Clemens, T. Graule, C.P. Bergmann, Photocatalytic activity of titania fibers obtained by electrospinning, *Mater. Res. Bull.* 44(2) (2009) 312-317.
- [54] F.A. Berutti, A.K. Alves, C.P. Bergmann, F.J. Clemens, T. Graule, Synthesis of CeO<sub>2</sub> and Y<sub>2</sub>O<sub>3</sub>-Doped CeO<sub>2</sub> Composite Fibers by Electrospinning, *Particul. Sci. technol.* 27(3) (2009) 203-209.

- [55] J. T. McCann, M. Marquez, Y. Xia, Melt coaxial electrospinning: A versatile method for the encapsulation of solid materials and fabrication of phase change nanofibers, *Nano Lett.* 6(12) (2006) 2868-2872.
- [56] J.E. Díaz, A. Barrero, M. Márquez, I.G. Loscertales, Controlled encapsulation of hydrophobic liquids in hydrophilic polymer nanofibers by co-electrospinning, *Adv. Funct. Mater.* 16(16) (2006) 2110-2116.
- [57] I.G. Loscertales, A. Barrero, I. Guerrero, R. Cortijo, M. Marquez, A.M. Gañán-Calvo, Micro/Nano encapsulation via electrified coaxial liquid jets, *Science* 295(5560) (2002) 695-1698.
- [58] D. Li, J.T. McCann, Y. Xia, M. Marquez, Electrospinning: A simple and versatile technique for producing ceramic nanofibers and nanotubes, *J. Am. Ceram. Soc.* 89(6) (2006) 1861-1869.
- [59] A.K. Moghe, B.S. Gupta, Co-axial electrospinning for nanofiber structures: preparation and applications, *Polym. Rev.* 48(2) (2008) 353-377.
- [60] M.R. Ismael, F. Clemens, P. Wyss, T. Graule, M.J. Hoffmann, N. Alford, Processing and properties of co-extruded lead zirconate titanate fibers, *J. Am. Ceram. Soc.* 95(1) (2012) 108-116.
- [61] C.L. He, Z.M. Huang, X.J. Han, L. Liu, H.S. Zhang, L.S. Chen, Coaxial electrospun poly(l-lactic acid) ultrafine fibers for sustained drug delivery, *J. Macromol. Sci. Part B Phys.* 45(4) (2006) 515-524.
- [62] Y. Zhuang, F. Li, G. Yang, Z. Xu, J. Li, B. Fu, Y. Yang, S. Zhang, A. Feteira, Fabrication and piezoelectric property of BaTiO<sub>3</sub> nanofibers, *J. Am. Ceram. Soc.* 97(9) (2014) 2725-2730.
- [63] D.P. Birnie, Esterification kinetics in titanium isopropoxide-acetic acid solutions, *J. Mater. Sci.* 35(2) (2000) 367– 374.
- [64] H. Yamamura, A. Watanabe, S. Shirasaki, Y. Moriyoshi, M. Tanada, Preparation of barium titanate by oxalate method in ethanol solution, *Ceram. Int.* 11(1) (1985) 17-22.

- [65] J. Yuh, L. Perez, W.M. Sigmund, J.C. Nino, Sol-gel based synthesis of complex oxide nanofibers, *J. Sol-Gel Sci. Technol.* 42(3) (2007) 323-329.
- [66] W. Maison, R. Kleeberg, R.B. Heimann, S. Phanichphant, Phase content, tetragonality, and crystallite size of nanoscaled barium titanate synthesized by the catecholate process: effect of calcination temperature, *J. Eur. Ceram. Soc.* 23(1) (2003) 127-132.
- [67] M.B. Smith, K. Page, T. Siegrist, P.L. Redmond, E.C. Walter, R. Seshadri, L.E. Brus, M.L. Steigerwald, Crystal structure and the paraelectric-to-ferroelectric phase transition of nanoscale BaTiO<sub>3</sub>, *J. Am. Chem. Soc.* 130 (2008) 6955-6963.
- [68] M. Yashima, T. Hoshina, D. Ishimura, S. Kobayashi, W. Nakamura, T. Tsurumi, S. Wada, Size effect on the crystal structure of barium titanate nanoparticles, *J. Appl. Phys.* 98(1) (2005) 014313.
- [69] Fu-Su Yen, Hsing-I Hsiang, Y.-H. Chang, Cubic to tetragonal phase transformation of ultrafine BaTiO<sub>3</sub> crystallites at room temperature, *Jpn. J. Appl. Phys.* 34(11) (1995) 6149-6155.
- [70] T. Hoshina, Size effect of barium titanate - fine particles and ceramics, *J. Ceram. Soc. Jpn.* 121(2) (2013) 156-161.
- [71] Y. Shiratori, C. Pithan, J. Dornseiffer, R. Waser, Raman scattering studies on nanocrystalline BaTiO<sub>3</sub> Part I—isolated particles and aggregates, *J. Raman Spectrosc.* 38(10) (2007) 1288-1299.
- [72] U.M. Pasha, H. Zheng, O.P. Thakur, A. Feteira, K.R. Whittle, D.C. Sinclair, I.M. Reaney, In situ Raman spectroscopy of A-site doped barium titanate, *Appl. Phys. Lett.* 91(6) (2007) 062908.
- [73] U.A. Joshi, S. Yoon, S. Baik, S.J. Lee, Surfactant-free hydrothermal synthesis of highly tetragonal barium titanate nanowires: A structural investigation, *J. Phys. Chem. B* 110 (2006) 12249-12256.

[74] A. Gajović, J.V. Pleština, K. Žagar, M. Plodinec, S. Šturm, M. Čeh, Temperature-dependent Raman spectroscopy of BaTiO<sub>3</sub> nanorods synthesized by using a template-assisted sol-gel procedure, *J. Raman Spectrosc.* 44(3) (2013) 412-420.

Table 1: Co-axial electrospinning parameters used in the present work.

Table 2: List of solutions with different compositions and viscosities, which were used as the shell solution for co-axial electrospinning.

Fig. 1: Schematic illustration of co-axial electrospinning and subsequent processes to achieve BT NT<sub>s</sub>.

Fig. 2: Viscosity values of different oils (core liquid) and shell solutions with different volume percent of PVP/Ethanol solutions with three different concentrations.

Fig. 3: SEM images of morphology and output diameter distribution of electrospun green NT<sub>s</sub> (after oil removing and drying) using different shell solutions (a) Sol 3 (b) Sol 4 (c) Sol 6 (d) Sol 7 (e) Sol 8.

Fig. 4: Change in the average outer diameter of electrospun green hollow fibers versus the viscosity of the shell solutions. The dashed line shows the viscosity of the core liquid (heavy mineral oil). The arrows indicates the viscosity range in which that the co-axial jet and hollow fibers were formed by the electrospinning.

Fig. 5: SEM images of morphology as well as output diameter distribution of calcined BT NT<sub>s</sub> obtained from (a): Sol 4 (b): Sol 7 and (c): Sol 8 at calcining temperature of 850 °C.

Fig. 6: SEM images of morphology as well as output diameter distribution of calcined BT NT<sub>s</sub> obtained from (a): Sol 4 (b): Sol 7 and (c): Sol 8 at calcining temperature of 1000 °C.

Fig. 7: TEM images of BT NT<sub>s</sub> obtained from (a) sol 4 and (b) sol 7 at calcining temperature of 1000 °C showing the morphology of highly porous NT<sub>s</sub> with nonuniform wall thickness.

Fig. 8: (a, b) TEM images of BT NT obtained from sol 8 and calcined at 850 °C showing the morphology of hollow structure with relatively uniform wall thickness (about 41 nm); (c): SAED patterns of different planes of cubic phase of BT; (d) HRTEM of BT NT<sub>s</sub> which shows lattice fringes.

Fig. 9: (a, b) TEM morphological images of BT NT obtained from sol 8 and calcined at 1000 °C showing wall thickness (about 38 nm); (c): SAED patterns showing some planes of tetragonal phase of BT; (d): HRTEM image of the intersection of two grains which shows lattice fringes.

Fig. 10: DSC-TGA thermograms of the electrospun BT NT<sub>s</sub> after oil removing in octane and drying (shell solution: sol 3) and nanofibers (NF<sub>s</sub>).

Fig. 11: XRD patterns of green and calcined BT NT<sub>s</sub> at different temperatures.

Fig. 12: Crystallite sizes and tetragonality values versus calcination temperature of electrospun BT NT<sub>s</sub> (using Sol 8 as the shell solution).

Fig. 13: Raman spectra of BT green (before calcining) and calcined NT<sub>s</sub>. The inset is spectra of green and calcined fibers up to 650 °C. The arrow denotes the band that could be assigned to rhombohedral phase. H indicates the band characteristic of hexagonal phase.

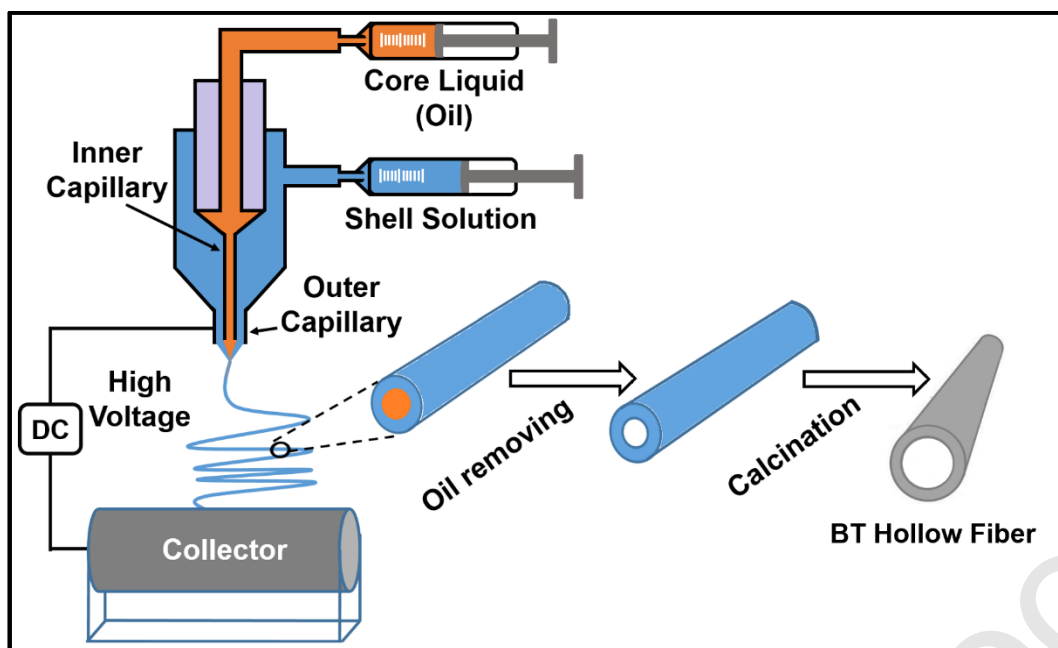


Fig. 1: Schematic illustration of co-axial electrospinning and subsequent processes to achieve BT NT<sub>s</sub>.

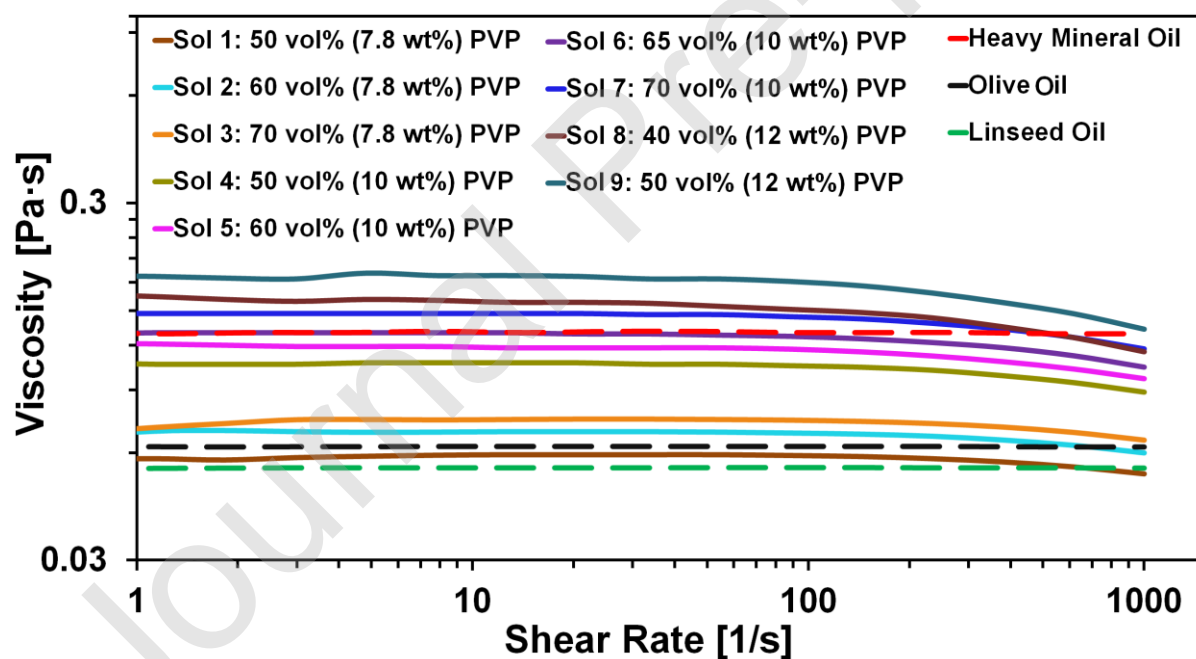


Fig. 2: Viscosity values of different oils (core liquid) and shell solutions with different volume percent of PVP/Ethanol solutions with three different concentrations.

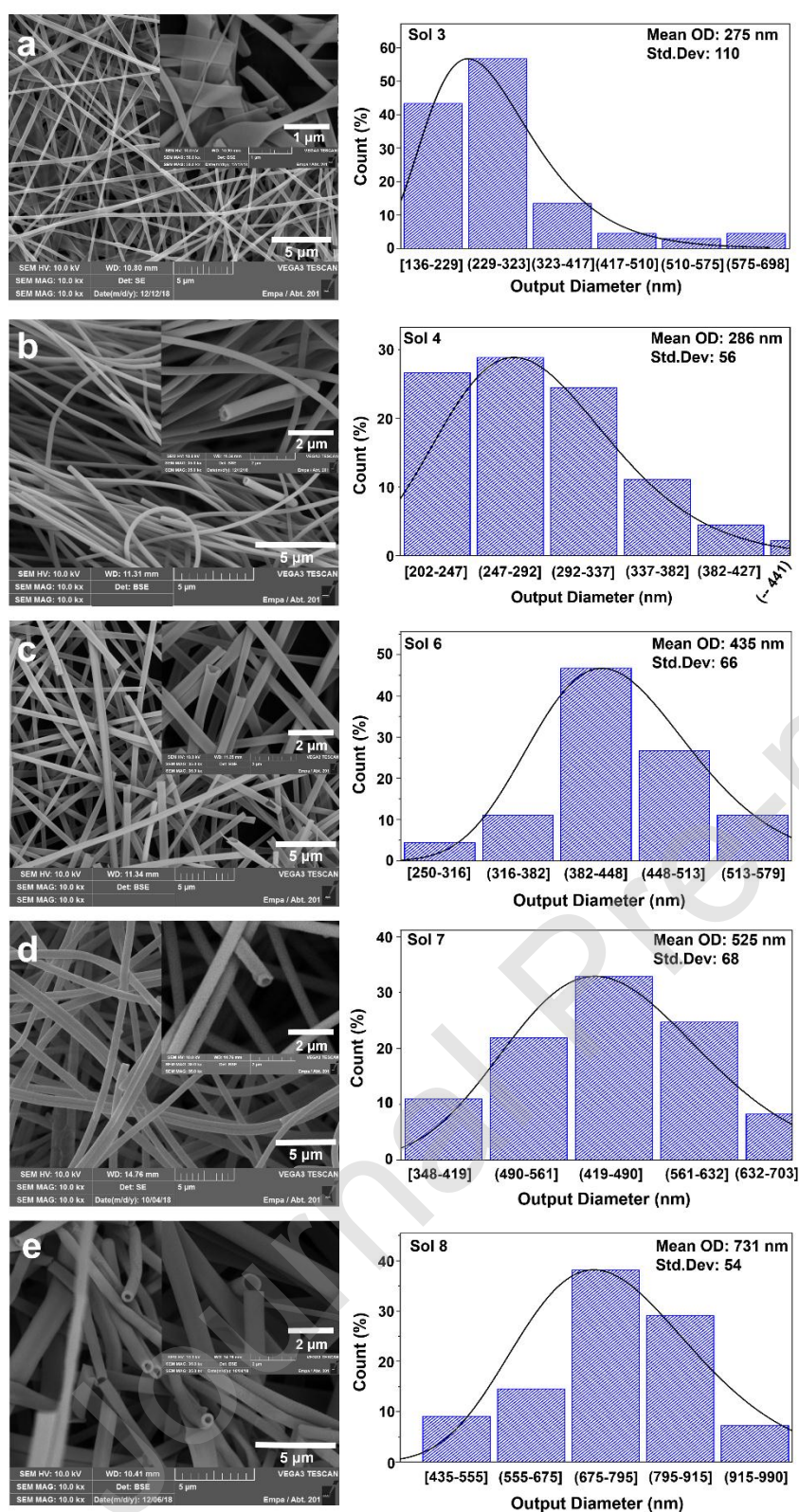


Fig. 3: SEM images of morphology and output diameter distribution of electrospun green NT<sub>s</sub> (after oil removing and drying) using different shell solutions (a) Sol 3 (b) Sol 4 (c) Sol 6 (d) Sol 7 (e) Sol 8.

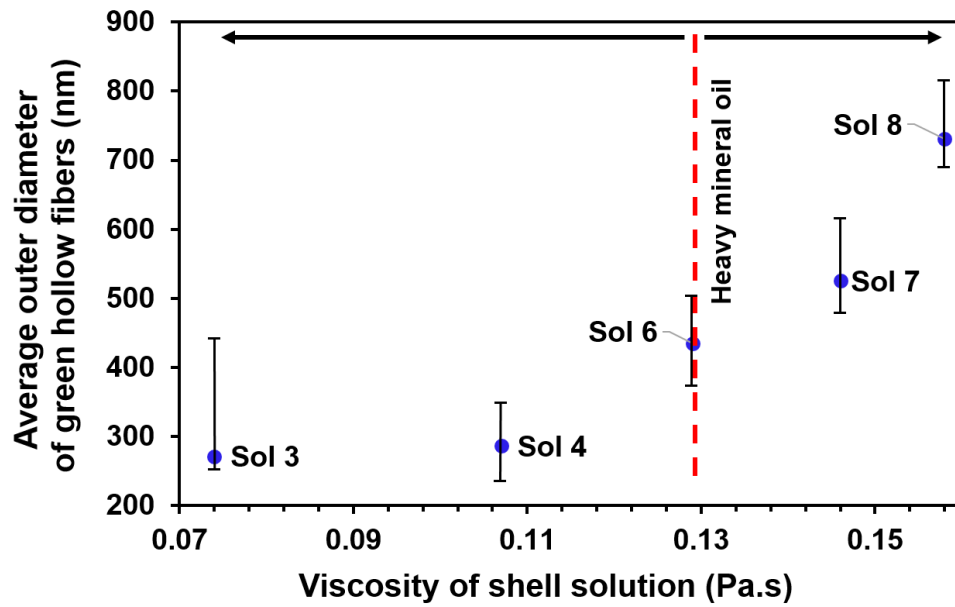


Fig. 4: Change in the average outer diameter of electrospun green hollow fibers versus the viscosity of the shell solutions. The dashed line shows the viscosity of the core liquid (heavy mineral oil). The arrows indicates the viscosity range in which that the co-axial jet and hollow fibers were formed by the electrospinning.

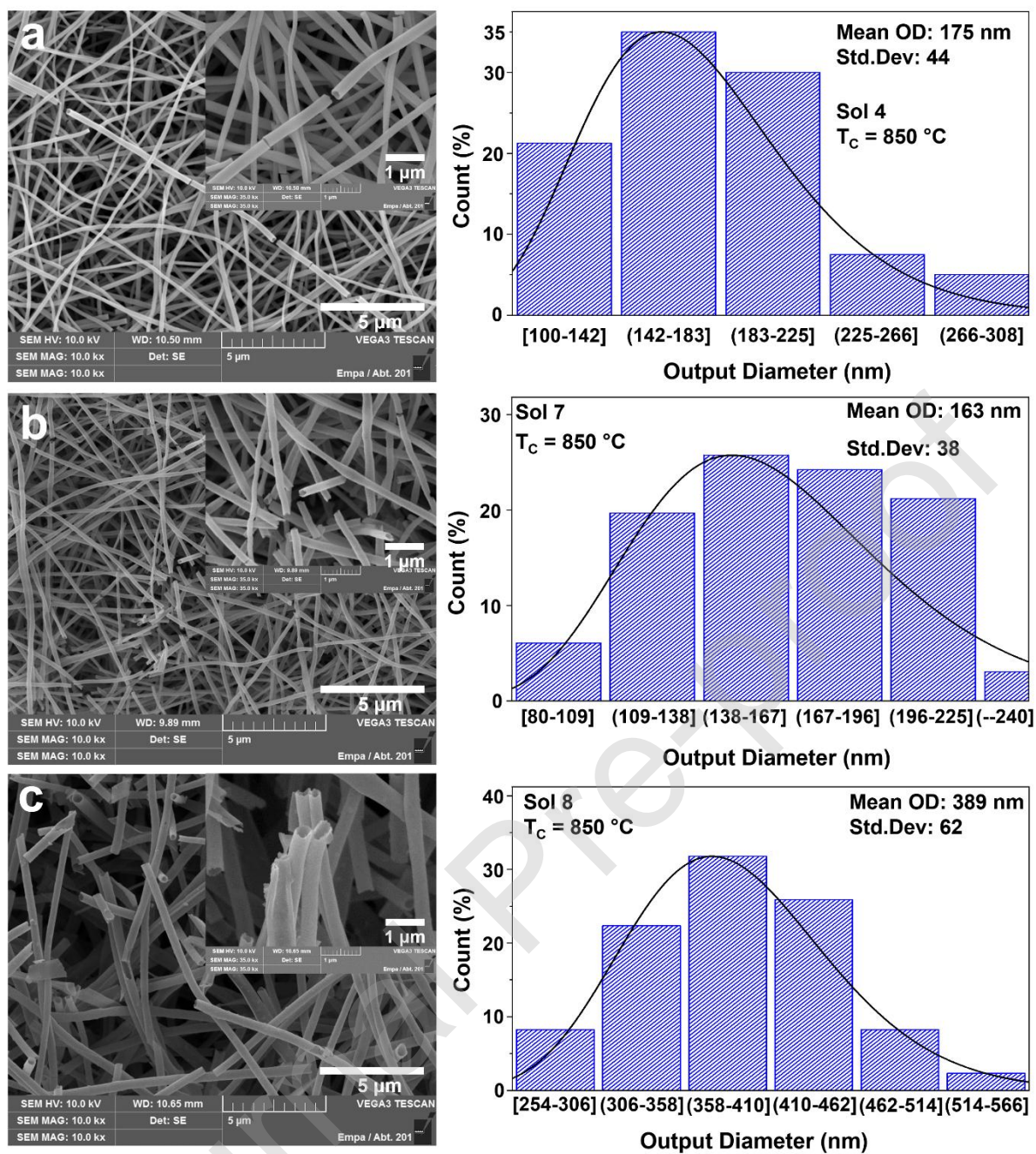


Fig. 5: SEM images of morphology as well as output diameter distribution of calcined BT NT<sub>s</sub> obtained from (a): Sol 4 (b): Sol 7 and (c): Sol 8 at calcining temperature of 850 °C.

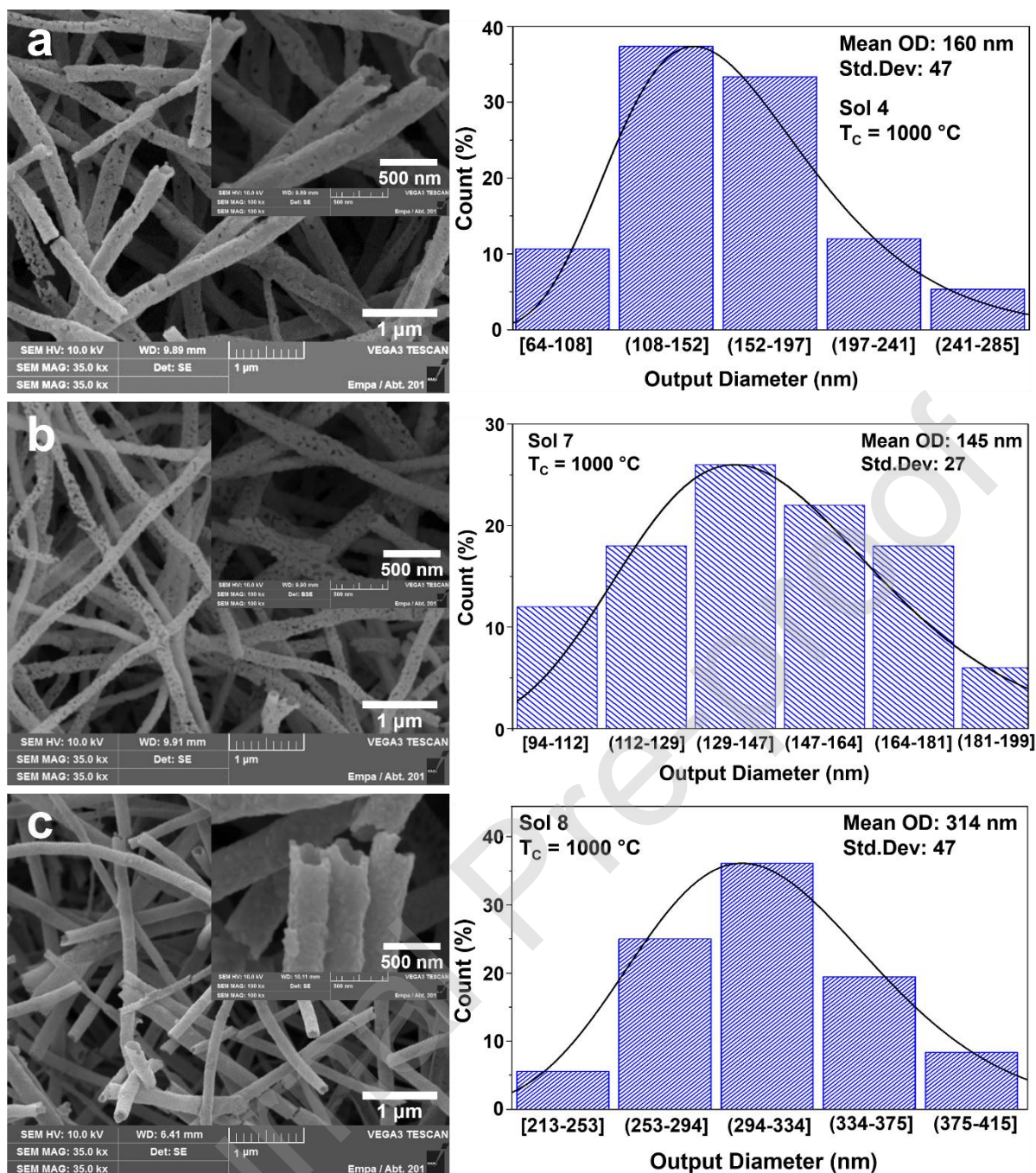


Fig. 6: SEM images of morphology as well as output diameter distribution of calcined BT NT<sub>s</sub> obtained from (a): Sol 4 (b): Sol 7 and (c): Sol 8 at calcining temperature of 1000 °C.

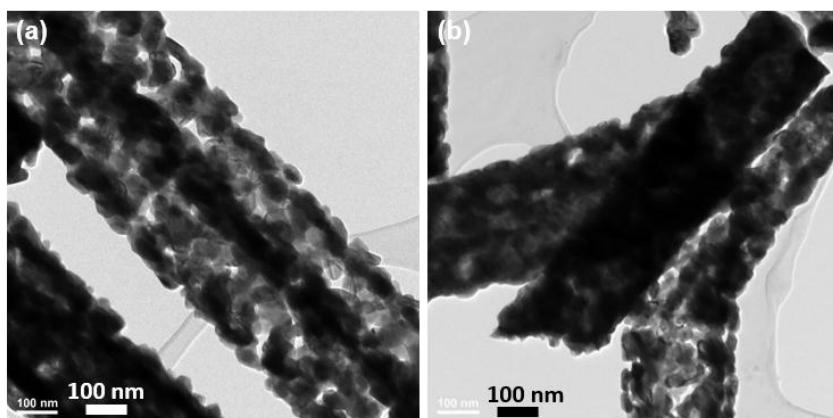


Fig. 7: TEM images of BT NT<sub>s</sub> obtained from (a) sol 4 and (b) sol 7 at calcining temperature of 1000 °C showing the morphology of highly porous NT<sub>s</sub> with nonuniform wall thickness.

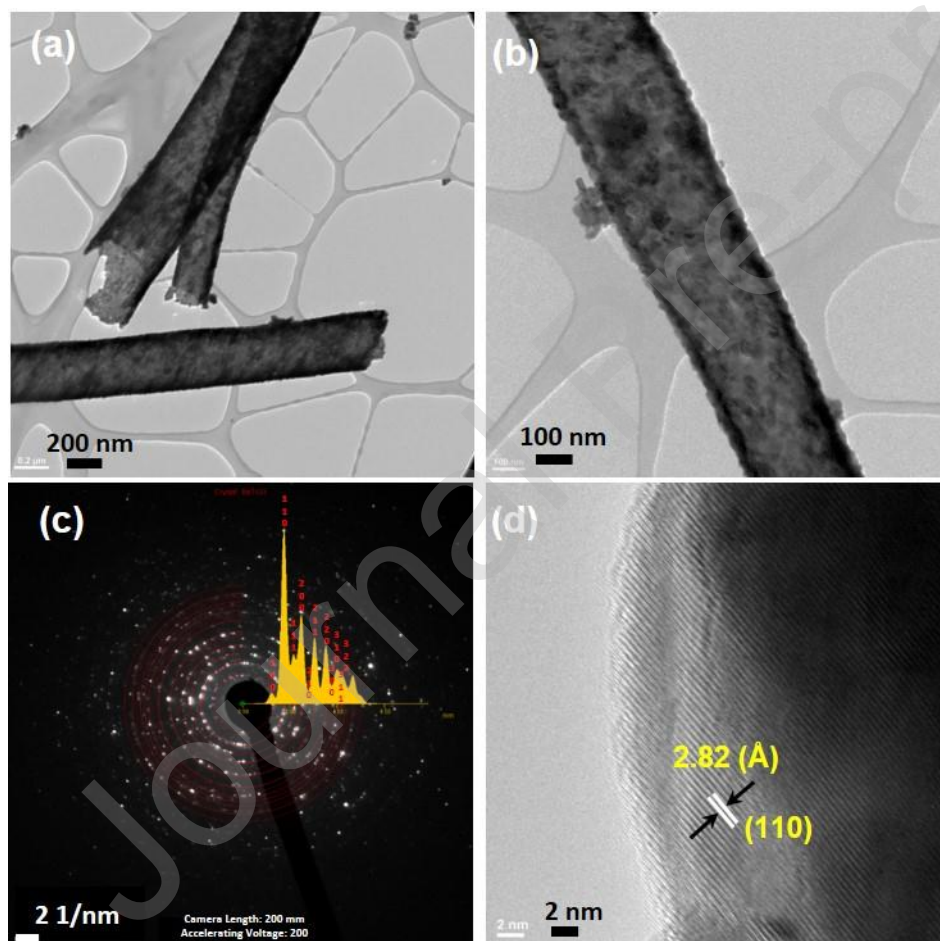


Fig. 8: (a, b) TEM images of BT NT obtained from sol 8 and calcined at 850 °C showing the morphology of hollow structure with relatively uniform wall thickness (about 41 nm); (c):

SAED patterns of different planes of cubic phase of BT; (d) HRTEM of BT NT<sub>s</sub> which shows lattice fringes.

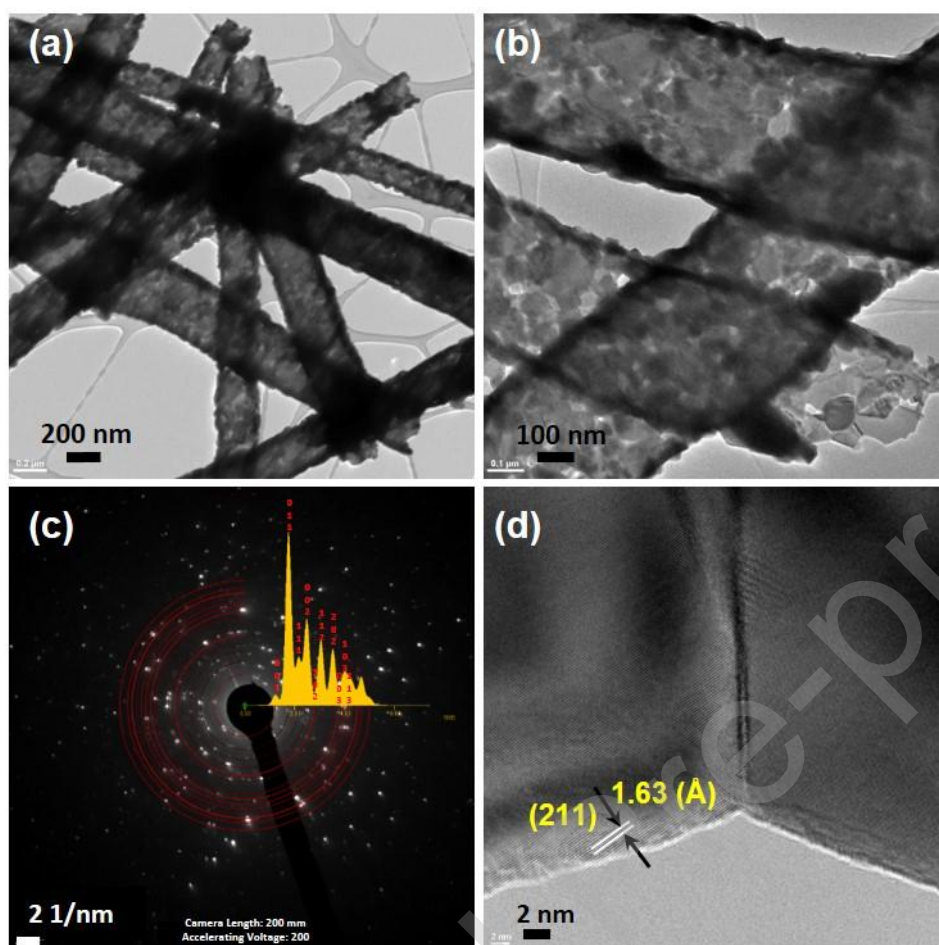


Fig. 9: (a, b) TEM morphological images of BT NT obtained from sol 8 and calcined at 1000 °C showing wall thickness (about 38 nm); (c): SAED patterns showing some planes of tetragonal phase of BT; (d): HRTEM image of the intersection of two grains which shows lattice fringes.

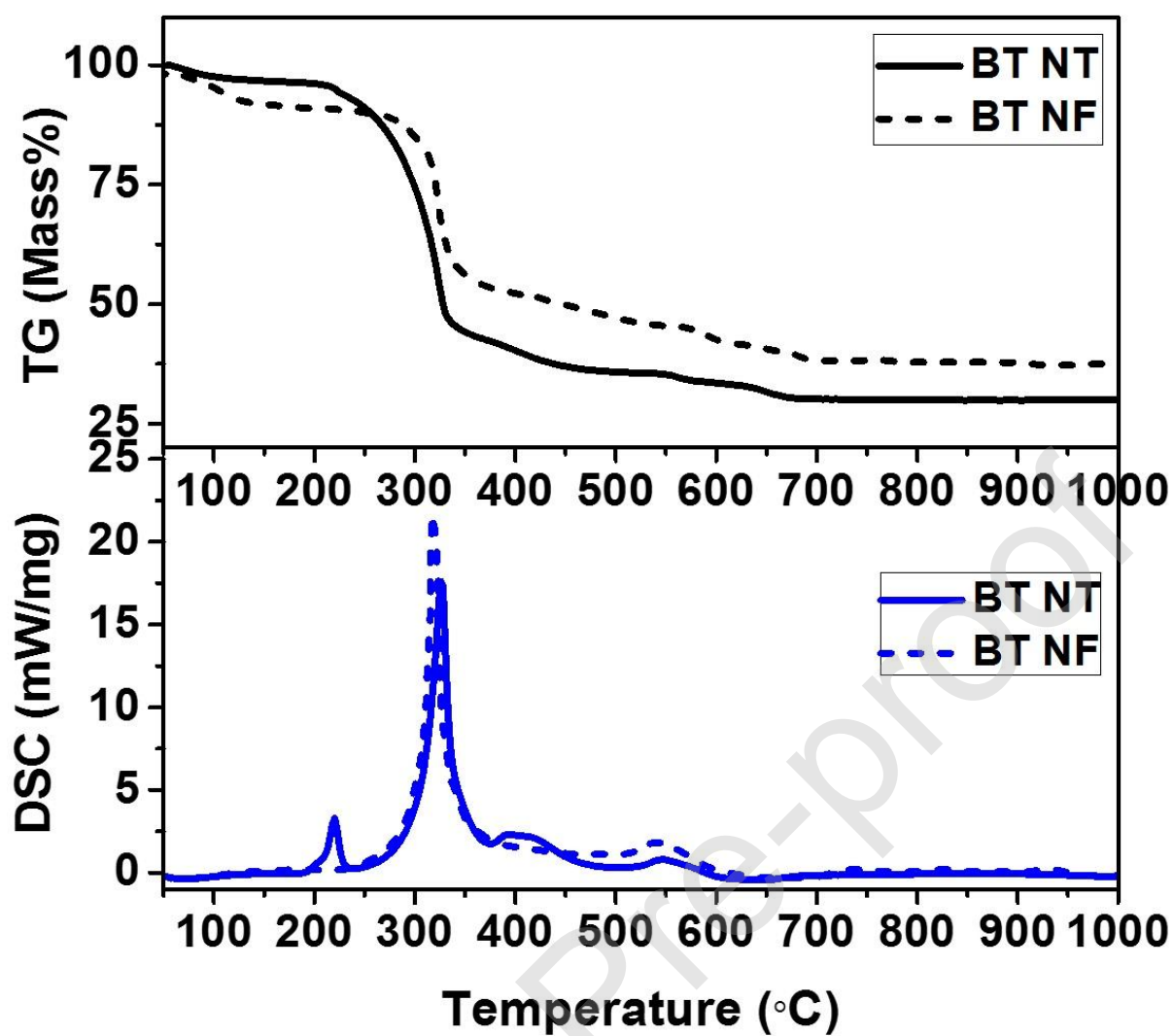


Fig. 10: DSC-TGA thermograms of the electrospun BT NT<sub>s</sub> after oil removing in octane and drying (shell solution: sol 3) and nanofibers (NF<sub>s</sub>).

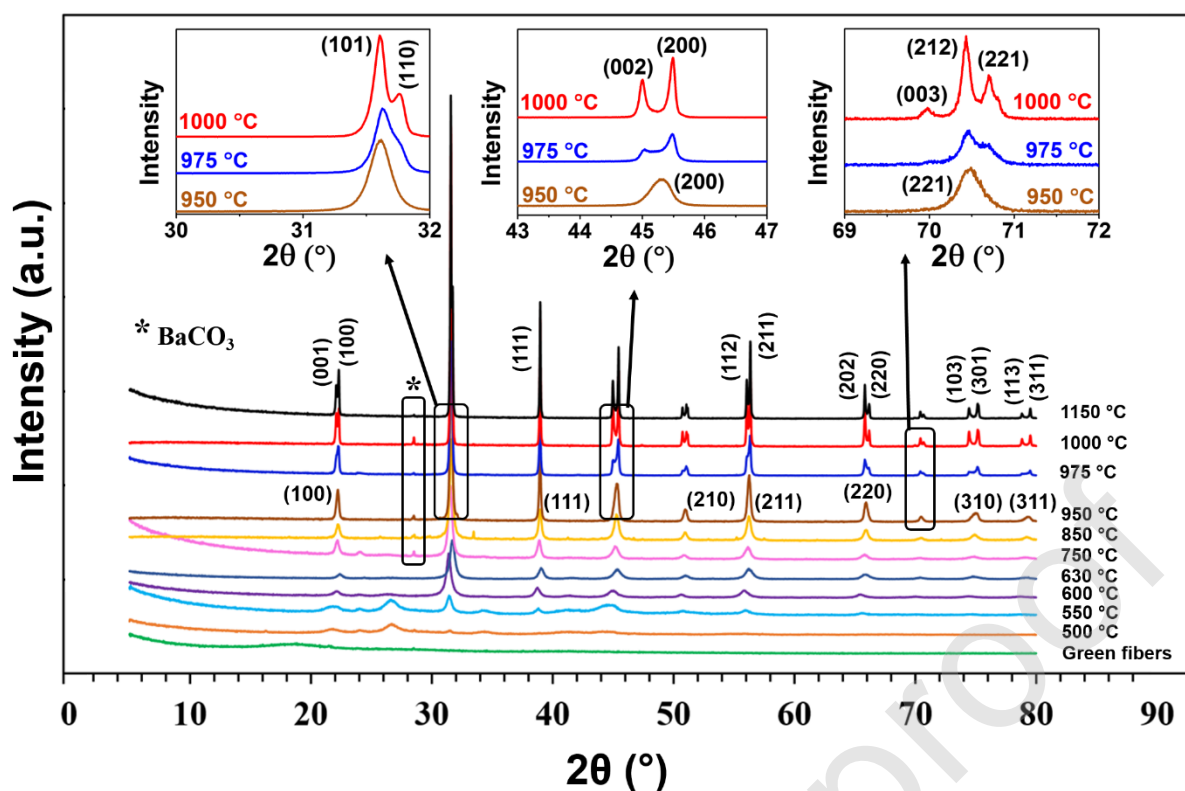


Fig. 11: XRD patterns of green and calcined BT NT<sub>s</sub> at different temperatures.

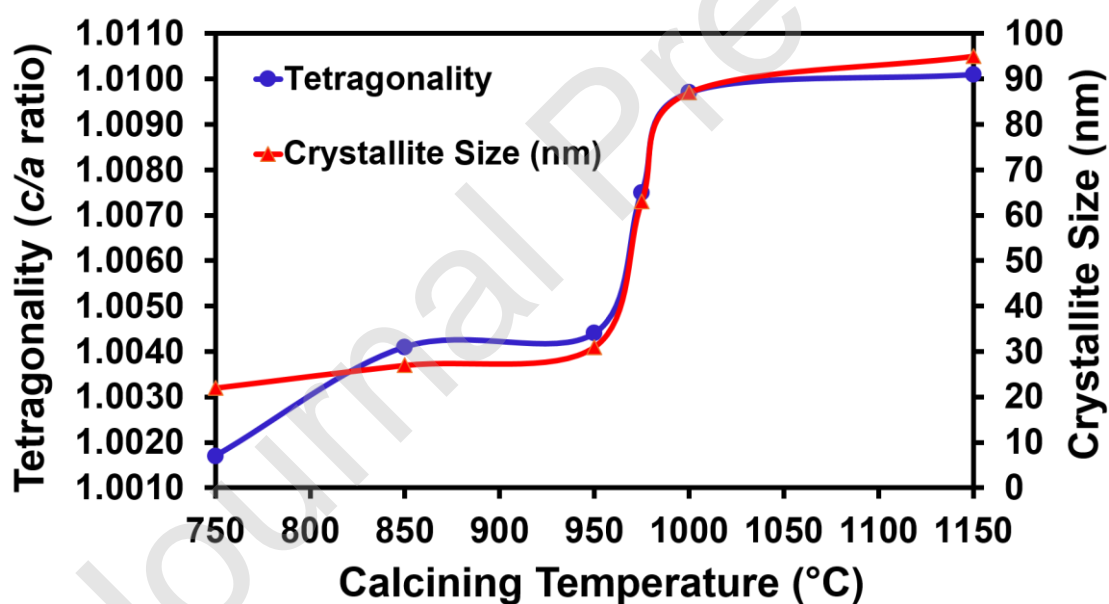


Fig. 12: Crystallite sizes and tetragonality values versus calcination temperature of electrospun BT NT<sub>s</sub> (using Sol 8 as the shell solution).

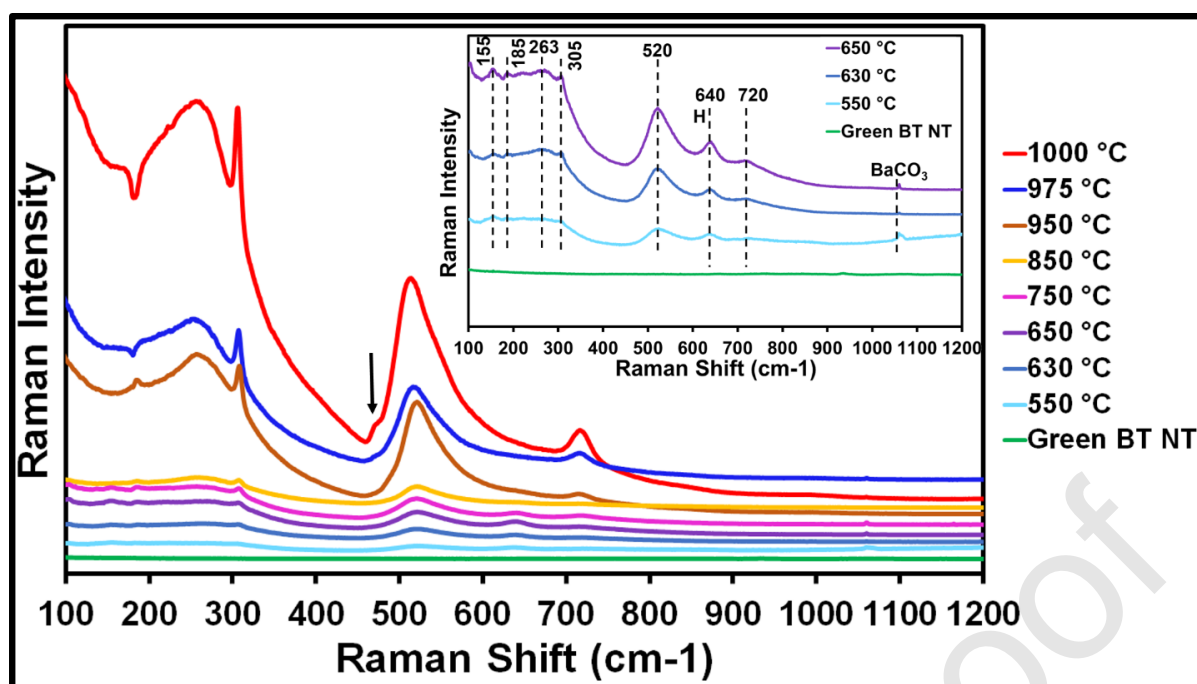


Fig. 13: Raman spectra of BT green (before calcining) and calcined NT<sub>s</sub>. The inset is spectra of green and calcined fibers up to 650 °C. The arrow denotes the band that could be assigned to rhombohedral phase. H indicates the band characteristic of hexagonal phase.

Table 1: Co-axial electrospinning parameters used in the present work.

Applied voltage (kv)	Nozzle to drum distance (cm)	Feeding rate (ml/h)		Drum speed (rpm)	Nozzle scan rate (mm/sec)	Temperature (°C)
		Shell solution	Core liquid			
17	10	0.3	0.1	10	2	23-25

Table 2: List of solutions with different composition and viscosities, which were used as the shell solution for co-axial electrospinning.

Shell solution No.	PVP/Ethanol (wt%)	vol% of PVP solution	Amount of PVP in Shell Solution (wt%)	Viscosity (Pa.s) (at shear rate: 10 s <sup>-1</sup> )	Viscosity ratio of shell to core solutions (at shear rate: 10 1/s)
Sol 1	7.8	50	3.01	0.062	0.48
Sol 3	7.8	70	4.21	0.074	0.57
Sol 4	10	50	3.75	0.107	0.82
Sol 6	10	65	4.88	0.129	≈1
Sol 7	10	70	5.25	0.146	1.12

Sol 8	12	40	3.47	0.158	1.22
Sol 9	12	50	4.46	0.188	1.49

Journal Pre-proof